DOI: 10.13009/EUCASS2017-149

Experimental and Numerical Evaluation of the Radiative Wall Heat Flux in the Post–Chamber of a Paraffin–Based Hybrid Rocket Engine

G. Leccese[⋆†], *D. Bianchi*[⋆] *and F. Nasuti*[⋆]
[⋆]*Sapienza University of Rome, Department of Mechanical and Aerospace Engineering*
Via Eudossiana 18, Rome, Italy 00184
giuseppe.leccese@uniroma1.it · daniele.bianchi@uniroma1.it · francesco.nasuti@uniroma1.it
K. J. Stober[*], *P. Narsai*[*] *and B. J. Cantwell*[*]
[*]*Stanford University, Department of Aeronautics and Astronautics*
496 Lomita Mall, Stanford, CA, USA 94305
stober@stanford.edu · pnarsai@stanford.edu · cantwell@stanford.edu
[†]Corresponding author: giuseppe.leccese@uniroma1.it

Abstract

The paper is intended to present both experimental and numerical approaches for estimating the heat exchange per thermal radiation towards the walls of lab–scale paraffin–based thrust chambers. Two firing tests of a lab–scale gaseous–oxygen/paraffin–wax hybrid rocket engine have been performed to apply such methods. In particular, the radiative wall heat flux has been evaluated by both spectroscopic measurements and discrete transfer method computations. Details of such approaches are given together with results achieved and suggestions for future improvements.

1. Introduction

In hybrid rocket engines (HREs) one of the propellants is stored at solid state and is physically separated from the other. Common HREs, in particular, rely on a solid fuel and a liquid or gaseous oxidizer. The latter propellant, injected into the grain port, reacts with the pyrolysis gas produced on the fuel grain surface. As a consequence, a diffusion flame, which in turn provides the convective and radiative heat flux needed to sustain the fuel pyrolysis process, is formed within the turbulent boundary layer.[9]

Hybrid rocket engines present several advantages against solid rocket motors and liquid rocket engines. With respect to solid rocket motors, HREs are characterized by safety during fabrication, storage and operations, by throttling, shutdown and restart capabilities, a lower sensitivity to ambient temperature and a higher specific impulse. Compared to liquid rocket engines, on the other hand, they exhibit a greater simplicity and reliability, lower costs and higher propellant densities. Besides the mentioned advantages, HREs can have environmentally clean exhausts, without ecologically damaging compounds, and can allow the introduction of various additives, for both performance and density enhancement. In addition, the large range of performance achievable by HREs, together with throttling capabilities, makes them suitable for a wide range of applications, from booster stages to in–space propulsion. There has been renewed interest in HREs in the last two decades for such reasons, making this class of rocket engines one of the envisaged options for future generation propulsion systems.[1]

Despite the advantages of HREs, together with the experience gained during several decades, this class of rocket engines has never been developed for launchers or space vehicles. This essentially occurred because of a poor understanding of physical phenomena inside the motor, together with some intrinsic drawbacks of HRE operations, such as the shift in mixture ratio, the low combustion efficiency and the low regression rate. Especially the latter, significantly limited the possibility to attain high thrust levels in an easy and effective manner and, accordingly, the technology readiness level of HREs.[1]

Nowadays, a very promising technique to solve the low regression rate problem relies on the use of paraffin–based fuels. In fact, it has been demonstrated that in paraffin–based HREs an hydrodynamically unstable liquid layer is formed on the fuel grain, leading to the entrainment of droplets into the gas stream.[17,18] Such an additional mass transfer mechanism acts like a continuous spray distributed along the port, with most of the fuel vaporization occurring

DOI: 10.13009/EUCASS2017-149

around droplets convecting between the melt layer and the flame front.[8] Because droplet entrainment is not limited by diffusive heat transfer to the fuel from the combustion zone, the mechanism is not limited by the blocking effect and leads to much higher regression rates than conventional polymeric fuels relying solely on pyrolysis. Regression rates from three to four times higher than the conventional values have been first observed in lab–scale motors and then confirmed in scale–up tests with different oxidizers.[19,20]

The technology development of the promising paraffin–based class of HREs requires a better understanding of physical phenomena occurring in the thrust chamber. The attention is focused here on the radiative heat transfer, which appears very important since it can contribute in a non–negligible way to the fuel regression. The diffusion flame formed in the boundary layer appears, in fact, an important source of radiative energy directed toward the fuel grain. Especially at low mass fluxes the relative contribution of thermal radiation is known to be more important because of the low values attained by the convective wall heat flux. Moreover, the radiative wall heat flux is expected to increase with both chamber pressure and port diameter for a given level of mass flux.[9] To date the subject of radiative heat transfer has been discussed predominantly, with different degrees of detail, for hydroxyl–terminated polybutadiene (HTPB) fueled HREs. Sankaran[31] predicted a radiative contribution up to 25% for lab–scales and further increases with motor dimensions. A radiative contribution ranging from 12% to 50% for different lab–scale firing tests has been estimated by Leccese *et al.*,[23] with possible over estimation due to slightly over predicted temperature fields. For the same test cases, Lazzarin *et al.*[21] showed a central role of the radiative wall heat flux in regression rate predictions, with contributions of approximately 50%. Serin *et al.*[32] finally highlighted a dominant contribution of the gas phase with respect to that of soot, predicting a 7% contribution due to thermal radiation.

To perform radiative heat transfer investigations a lab–scale gaseous–oxygen/paraffin–wax HRE designed and built at Stanford University has been tested at 17.2 bar nominal chamber pressure with different fuel–rich mixture ratios.[28] During firings the emission spectra from the combustion gases have been gathered at mid post–chamber location thanks to a spectrometer fastened into an optical port fabricated for the purpose.[34] The spectrum of absolute irradiance at mid–burning time has been fitted with Planck's law and then integrated over wavelengths providing an indirect experimental measurement of the radiative wall heat flux. At the same time, an in–house radiative code developed at Sapienza University of Rome has been employed to compute the radiative wall heat flux in the point of interest. The radiative code allows the integration of the radiative transfer equation (RTE) within gray/diffuse axisymmetric walls containing gray/non–scattering inhomogeneous media. The integration strategy relies on the discrete transfer method (DTM),[25] based on a combined discretization of solid angles and line–of–sights. The flow field local conditions needed by the radiative code are taken from computational fluid dynamic (CFD) simulations of firing tests, performed with an in–house developed Reynolds–averaged Navier–Stokes (RANS) solver properly adapted to the case of HREs using paraffin–wax as fuel.[22]

Both experimental and numerical results are presented and discussed. Focus is also given to the data reduction procedure, to evaluate radiative wall heat fluxes from emission spectra, and CFD solutions supporting DTM computations. Although large uncertainty remains in the radiative wall heat flux estimation, the basics of a combined approach of experimental diagnostic and numerical simulation is presented in this work.

2. Experimental setup

The experimental setup is represented by the lab–scale gaseous–oxygen/paraffin–wax HRE shown in Fig. 1, previously fully described,[29] and originally designed and constructed for the purpose of conducting erosion rate and wall heat flux measurements at nozzle throat.

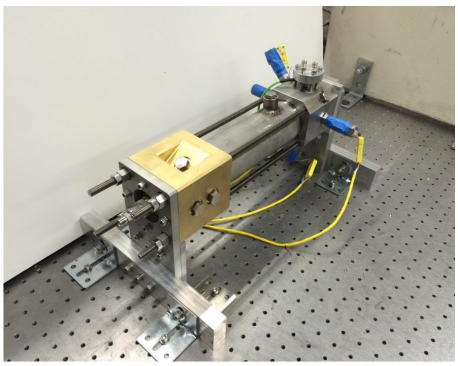

Figure 1: View of the thrust chamber with associated hardware.

DOI: 10.13009/EUCASS2017-149

The fuel formulation consists of a mixture of 342 K melting temperature paraffin–wax and stearic acid in the proportions of 98% and 2% by mass, respectively. The stearic acid has been added to increase the structural integrity of the fuel grain, showing to have a favorable impact on combustion stability. Trace amounts of sodium chloride salt, less than 1% by mass, have been sometimes added for testing emission spectra analyses. Fuel grains were spin casted, accommodating burn times up to six seconds.

The location for spectral acquisition has been set at the mid post–chamber because, with the exception of the fuel surface, it provides the most insight into radiative heat transfer as a mechanism for liquefying the fuel. In order to accommodate spectral acquisition from the post–chamber, a new combustion chamber has been fabricated with an optical port opposite to the aft–end pressure port. The optical port, whose schematic is presented in Fig. 2, consists of a window holder welded onto the post–chamber and equipped with a bung. The window holder envelops a 25.4 mm diameter and 5 mm thickness sapphire window, which is sealed and supported by three o–rings. The window is fully transparent from ultraviolet to near–infrared wavelengths and ensures no birefringence on transmitted radiation in this range. A 6.35 mm diameter hole is cut into the bung to flush against the window the fiber optic cable of the adopted FLAME–S Ocean Optics spectrometer. To look into the post–chamber, holes are cut also into the chamber wall, with the same diameter, and into both the aft insulation and the thermal protection, with a larger diameter of 9.53 mm. Spectra are gathered with a sampling frequency of 10 Hz. Wavelengths between 0.1 and 1.1 μm, so covering parts of the ultraviolet, visible, and near–infrared spectral domains, are inspected. However, initial tests suggested that portions of the spectra above 0.9 μm lacked fidelity due to the limitations of the diffraction grating within the spectrometer at these wavelengths. Therefore, only data in the range of 0.1–0.9 μm are actually considered.

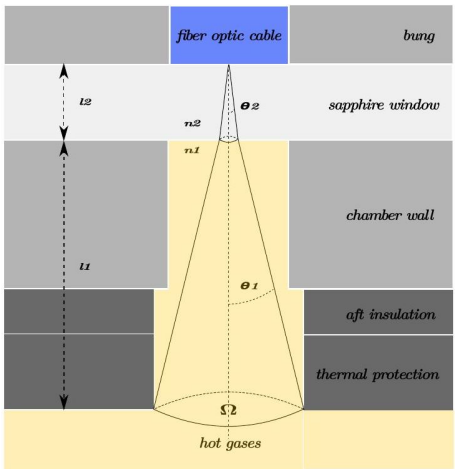

Figure 2: Optical port and relevant field of view schematic.

The geometry described in Fig. 2 affects the spectrometer field of view (FOV) into the post–chamber, with the radiation crossing two different media before reaching the core of the optical fiber: the gas between the wall components and the window. A refractive index $n_1 = 1$ is assumed for the gaseous layer, while its thickness $l_1 = 19.24$ mm is obtained as the sum of the aft insulation, thermal protection and chamber wall thicknesses. An average refractive index across wavelengths under scrutiny, $n_2 = 1.768$, is considered within the window of thickness $l_2 = 5$ mm. By taking into account refraction effects *via* Snell's law[27] the FOV semi–aperture angles within each layer is evaluated as $\theta_1 = 11.7$ and $\theta_2 = 6.6$, respectively.

3. Numerical model

The numerical model relies on the integration of the RTE under the hypotheses of axisymmetric gray/diffuse boundaries and inhomogeneous gray/non–scattering media. The gray assumption is quite accurate for the wall, because of its continuous behavior over the spectrum, while allowing for a significant reduction in computational time, by means of a global treatment of spectral features, when introduced for the medium. The constraint on computer time, in fact, almost invariably restricts the choice to gray gas approaches, which assume that the optical properties of the medium are independent of radiation frequency, thereby enabling to describe the phenomenon in terms of a single radiative intensity, rather than a huge number of spectral intensities. The high roughness level expected for the wall surface, is well in agreement with the diffuse wall hypothesis, since reflection from rough surfaces approximates the diffuse reflection regime.[16] The non–scattering nature of soot[27] and the absence of other solid particles suspended in the gas

DOI: 10.13009/EUCASS2017-149

phase, finally, agrees with a non–scattering behavior of the medium. It is also assumed that radiation does not affect the flow field significantly,[24] because of the relative small weight of the wall heat transfer, and in particular of the radiative contribution, as compared to the whole thermal power generated within the thrust chamber. This obviates the need to calculate radiative heat flux at each cell center in the flow field, neglecting its contribution into the energy conservation equation, and therefore to perform its evaluation only along the wall boundary.

The radiative wall heat flux is defined by the following integral of the radiative intensity at wall I_w over the hemispherical solid angle Ω facing the incoming radiation:

$$\dot{q}_{w,\mathrm{rad}} = \int_{2\pi} I_w \sin\theta \, d\Omega = \int_0^{2\pi} \int_0^{\frac{\pi}{2}} I_w \sin\theta \cos\theta \, d\theta \, d\psi \tag{1}$$

where θ and ψ are the elevation and azimuth angle, corresponding to a generic line–of–sight within the hemispherical solid angle, respectively.

The radiative intensity at wall from a generic line–of–sight can be computed by integrating the RTE along the whole radiation path length. The RTE expresses the balance of radiative intensity along a generic direction, including contributions due to absorption/emission and, potentially, in/out–scattering. Under the assumption of gray/non–scattering medium it reduces to the form:

$$\frac{dI}{ds} = j^e - \kappa I = \kappa I_b - \kappa I \tag{2}$$

with I the radiative intensity, s the coordinate along the line–of–sight, κ and j^e the absorption and emission coefficients, respectively.

The RTE formal solution is given by,

$$I_w = I_0 \, \exp\left(-\int_{s_0}^{s_w} \kappa \, ds\right) + \int_{s_0}^{s_w} j^e \, \exp\left(-\int_s^{s_w} \kappa \, ds'\right) ds \tag{3}$$

where it is assumed that the line–of–sight originates from another wall point. The radiative intensity I_w reaching a generic wall point s_w from a given line–of–sight is therefore due to the contributions I_0 from the origin of the line–of–sight s_0, and j^e from each point in the medium along the line–of–sight s. The exponential terms account for radiation absorption by the medium from the origin, in the first term, and through the medium itself, in the second term. Equations (1–3) require the radiative intensity at the origin and the absorption coefficient. The emission coefficient is in fact a function of the previous one according to Eq. (2).

The radiative intensity at the origin, under the assumption of gray/diffuse wall, assumes the form:

$$I_0 = \frac{\epsilon_0 \sigma T_0^4 + \rho_0 \dot{q}_{0,\mathrm{rad}}}{\pi} \tag{4}$$

including the radiative intensity emitted and reflected by the wall, according to a certain surface emissivity ϵ_0 and surface reflectivity ρ_0.

The absorption coefficient is derived by means of a global model, typically used for high–temperature combustion mixtures under vibrational equilibrium conditions,

$$\kappa_g = p \sum_{i=1}^{N_{\mathrm{rad}}} X_i \kappa_{p,i} \tag{5}$$

indicating that the absorption of radiative energy is proportional to the pressure p, i.e. the number of molecules per unit volume, and to the absorption coefficients of the N_{rad} participating species, weighted with their concentrations in terms of molar fractions X_i. In particular, water vapor, carbon dioxide and carbon monoxide are most relevant in the process of thermal radiation exchange.[36] The absorption coefficients of the participating species, known as Planck–mean absorption coefficients, are averaged over the whole spectrum. Their temperature dependence is given up to 2800 K by Giordano and Lentini,[13] fitting the curves reported in Modest.[27] Rivière and Soufiani[30] described an updated model for the Planck–mean absorption coefficients up to 5000 K, see Fig. 3, which is adopted here.

In the present work the RTE is integrated via DTM according to a suitable developed code. The DTM foresaw the evaluation of the radiative heat flux at a selected calculation point on the wall by solving the RTE along representatively directed beams of radiation emanated from the calculation point under scrutiny within the envisaged enclosure. The equations of the problem are written in finite form by discretizing the domain and hence substituting the integration operation with relevant summations. The solid angle seen by the generic calculation point is discretized into different sectors by suitably dividing the elevation and azimuth angles with which it is represented. In particular, the range of the elevation angle θ_{ij}, between 0 and $\pi/2$, is subdivided into I intervals while that of the azimuth angle ψ_{ij}, between 0

DOI: 10.13009/EUCASS2017-149

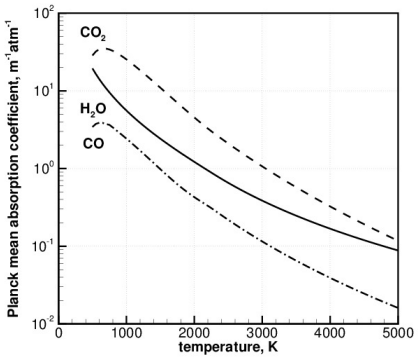

Figure 3: Planck–mean absorption coefficients for water vapor, carbon dioxide and carbon monoxide.[30]

and 2π, into J intervals. In such a way a finite number $I \times J$ of rays ij, each representing a sector of the solid angle, is extracted from the calculation point. The path length of each ray defined along the abscissa s_{ij} is in turn discretized into a number of L_{ij} intervals in order to perform a finite integration of the RTE and hence evaluate the radiative wall heat flux in the location of interest. In particular, the integration over the path length along each ray allows the evaluation of the relevant radiative intensity at wall $I_{w,ij}$:

$$I_{w,ij} = I_{0,ij} \exp\left(-\sum_{l=1}^{L_{ij}} \kappa_l \Delta s_l\right) + \sum_{l=1}^{L_{ij}} j_l^e \exp\left(-\sum_{m=l}^{L_{ij}} \kappa_m \Delta s_m\right) \Delta s_l \tag{6}$$

while the integration over the solid angle at each calculation point allows the evaluation of the associated radiative wall heat flux $q_{w,rad}$:

$$\dot{q}_{w,\mathrm{rad}} = \sum_{i=1}^{I} \sum_{j=1}^{J} I_{w,ij} \sin\theta_{ij} \cos\theta_{ij} \, \Delta\theta_{ij} \, \Delta\psi_{ij} \tag{7}$$

where Eqs. (6,7), are the discretized form of Eqs. (3,1), respectively.

The field and wall local conditions needed by the method can be recovered from CFD simulations, with which DTM computations are coupled. In particular, the pressure, temperature and molar fraction fields are required to evaluate the absorption coefficient at each space step along each line–of–sight according to Eq. (5). The wall temperature is also required to evaluate the radiative intensity at the origin of the line–of–sight by applying the boundary condition in Eq. (4). Since such boundary conditions depend on the radiative power flux reflected by the wall, then on the incoming radiative intensity, an iterative computational procedure is required by the method.

Computational fluid dynamics simulations of the envisaged paraffin–based HRE, to support DTM computations, are performed by integrating RANS equations through a suitable in–house developed solver for three-dimensional, turbulent, compressible, multi–component and reacting flows of thermally perfect gases.[3] The solver adopts a second order accurate in space finite volume Godunov formulation, with a Roe approximate Riemann solver for multi–block structured meshes. Time integration uses the Strang operator–splitting technique,[35] with convective and diffusive terms integrated by a second–order Runge–Kutta scheme, whereas for the chemical source term a stiff ordinary differential equation (ODE) implicit integrator is used.[6] The Spalart–Allmaras one–equation model[33] is used to compute the turbulent viscosity. Both turbulent thermal conductivity and turbulent mass diffusivity are computed from turbulent viscosity, turbulent Prandtl and Schmidt numbers and specific heat at constant pressure. The thermodynamic and transport properties of each species are approximated by seventh and fourth-order polynomials of temperature, respectively.[14] Mixture viscosity and conductivity are derived from the Wilke's rule.[2] The chemical reactions are modeled via finite–rate chemistry. A seven reactions and ten species global mechanism is used to model the combustion process between gaseous oxygen and paraffin–wax. In particular, a thermal cracking reaction for paraffin–wax into ethylene,[5] assumed as the representative cracking product, is coupled to a global mechanism for butadiene,[10] adapted here to the case of ethylene in terms of stoichiometric coefficients, leaving unaltered the reaction rates. Notice that in the present test campaign, as it typically happens in hybrid rocket conditions, the melted paraffin–wax appears in the supercritical pressure regime, thus behaving like a dense fluid. For such a reason paraffin–wax thermophysical properties are assumed to be those at liquid state,[26] although they are used in a thermally perfect gas model. This approximation can be considered fairly good below the critical temperature, when the fluid actually tends to behave like a liquid.

DOI: 10.13009/EUCASS2017-149

4. Test cases

For the radiative wall heat flux analysis two firing tests have been performed. Different graphite nozzles have been used, each with a different throat area, in order to enable the same chamber pressure of 17.2 bar, with different oxidizer mass flow rates. Values of 0.05 and 0.09 kg/s are considered, corresponding to expected mixture ratios of 2.10 and 2.75, respectively. Notice that the stoichiometric mixture ratio is 3.45, indicating that all firing tests have been run fuel–rich. Such conditions lead to the expectation of soot formation during combustion and subsequent continuous emission per condensed phase in the spectra.

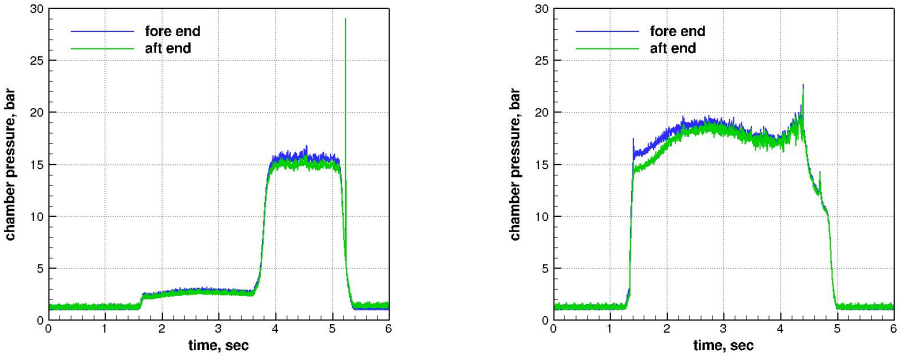

(a) test case 1 (b) test case 2

Figure 4: Recorded pressures at fore and aft–section.

During each firing test, the chamber pressure, at fore and aft–end sections, and the oxidizer mass flux, are acquired. In Fig. 4 the pressure traces measured at motor fore and aft–end are shown for both the envisaged test cases. Changes in the fuel grain mass and end–section diameter are also measured. The latter data, together with the burning time estimated from the pressure traces, allow the calculation of the regression rate via mass loss method.[4] The achieved test conditions, as shown in terms of time–averaged quantities in Table 1, slightly differ from the nominal desired values, because of the uncertainty on regression rate before firing tests. In particular a lower pressure in test condition 1 and a lower mixture ratio in test condition 2 with respect to nominal values stand out.

Table 1: Achieved time–averaged test conditions.

TC	t_b, s	D_p, mm	G_o, kg/m^{2}s	O/F	p_c, bar	$\dot{r}$, mm/s	c^*, m/s	η_{c^*}
1	1.41	25.39	100.15	2.17	14.85	1.98	1514.4	0.82
2	3.10	27.01	147.60	1.74	17.05	3.86	1622.5	0.88

5. Data reduction

Before starting the data reduction procedure, the emission spectrum at mid burning time is properly selected among the spectra gathered along the whole burn. This appears necessary to make the comparison with numerical results consistent, since numerical simulations are performed at mid burning time to enforce the measured time–averaged regression rate as inflow boundary condition at wall.

Once the emission spectrum at mid burning time E_λ is extracted it can be simply integrated over wavelengths λ to obtain the experimental radiative wall heat flux in the point under scrutiny:

$$\dot{q}_{w,\mathrm{rad}} = \int_0^\infty E_\lambda \, d\lambda \tag{8}$$

Actually, some modifications are needed to such apparently straightforward procedure in order to make reasonable comparison between experimental and numerical evaluations.

Firstly, while the numerical model is calibrated over almost the whole infrared domain, to which belong the majority of wavelengths responsible of the heat exchange per thermal radiation, the employed spectrometer includes

DOI: 10.13009/EUCASS2017-149

only a small band in the near infrared range, because it is devoted also to visible and ultraviolet analyses. In order to infer information about the content of higher wavelengths and to properly evaluate the radiative wall heat flux from the experimental data, the measured emission spectrum is fitted with Planck's law:[27]

$$E_\lambda = \frac{C_1}{\lambda^5 (e^{\frac{C_2}{\lambda T}} - 1)} \tag{9}$$

where $C_1 = 3.742 \times 10^{-16}$ W m^2 and $C_2 = 1.439 \times 10^{-2}$ m K. For such fit, care is taken to avoid regions of the spectrum with emission peaks. In particular, since data between 0.5–0.7 μm are generally found to be associated with purely continuous gray–body emission, only this range is considered. Normalized spectra with respect to the spectral emissive power at 0.7 μm are fitted with a black–body spectrum, also exhibiting a magnitude of one at 0.7 μm, by varying the value of the candidate temperature. The square error is summed across all wavelengths in the envisaged interval and minimized to determine the temperature ensuring the best fit. Once temperature is determined the shape of the spectrum is also uniquely found. This is not the case of the magnitude that, instead, can be found by suitably scaling a black–body spectrum obtained with the selected temperature to fit the dimensional gathered spectrum. Notice that due to the data normalization, the described approach works not only for black–body but also for gray–body emissions.

Secondly, both the FOV limitation and the transmission through the gas and window layers needs to be taken into account on the numerical side, see Fig. 2. The FOV limitation is enforced in the computations by constraining the line–of–sight elevation angle θ_{ij}, between $\pi/2 - \theta_1$ and $\pi/2$, hence by reducing the solid angle to about $\Omega = 0.131$ sr. The transmission through the gas and window layers is taken into account by multiplying the computed radiative wall heat flux by the transmittance of each layer, evaluated via Beer's law[27] by considering a proper absorption coefficient and mean path length:

$$\tau_i = \exp\left(-k_i \frac{l_i}{\theta_i} \int_{\frac{\pi}{2}-\theta_i}^{\frac{\pi}{2}} 1 + \tan\left(\frac{\pi}{2} - \theta\right) d\theta\right) \tag{10}$$

For the hot gas in the hole the absorption coefficient is evaluated through Eq. (5) by considering the properties in the cell of the CFD domain facing the hole for spectroscopy measurements. Values of 23.71 and 25.68 m^{-1} are determined for test case 1 and 2, respectively. The absorption coefficient of the window is, on the other hand, known from the window data sheet to be equal to 32.50 m^{-1}. Transmittance of 0.605 and 0.579 for the gas layer, respectively for test case 1 and 2, and of 0.842 for the window layer come out and are accordingly used in the computation.

6. Results and discussion

The gathered emission spectra at mid burning time, i.e. 4.50 and 2.85 s from the beginning of data recording for test case 1 and 2, respectively, are shown in Fig. 5.

According to the procedure previously described, fitting the spectra in Fig. 5 with Planck's law leads to the choice of a proper flame temperature, describing the shape of the fitting curve, whose values are presented in Table 2.

The results of the fitting procedure with Planck's law are shown in Fig. 6. The spectral interval taken into account ranges all along the infrared domain, from 0.1 to 1000 μm. The major contributions of emission are however located in the near and middle–infrared, between 1 and 10 μm.

The integration over wavelengths of spectral emissive power distributions leads to the values of wall heat flux shown in Table 3.

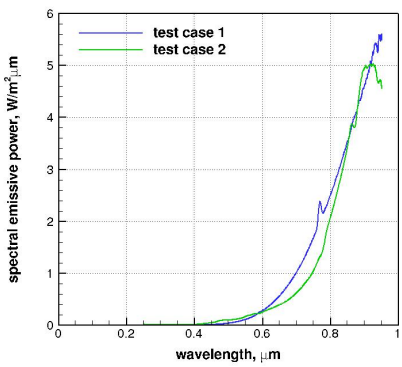

Figure 5: Gathered spectra at mid burning time.

DOI: 10.13009/EUCASS2017-149

Table 2: Flame temperature and medium emissivity from fitting procedure.

TC	$T_{c,fit}$, K
1	1650.4
2	1826.0

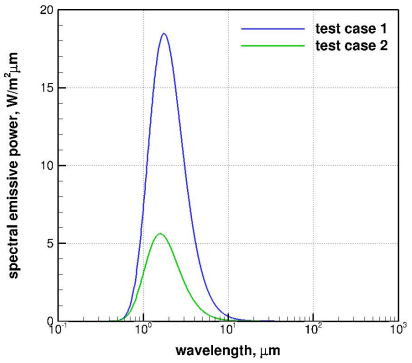

Figure 6: Fit of experimental spectral emissive power with Planck's law.

Table 3: Measured radiative wall heat fluxes.

TC	$q_{w,rad}$, W/m^2
1	49.33
2	13.56

In the CFD axisymmetric simulations, the details of the pre and post–chamber cavities have been omitted to allow relatively modest grid sizes. The adopted geometrical simplification of constant cross section has been found to be a fair assumption by Bianchi *et al.*[4] A grid of 170×60 elements, respectively in the axial and radial directions, has been selected. A proper grid refinement at the edges of the fuel grain and in the near–wall regions has also been introduced in order to capture the fuel injection location and the phenomena occurring into the boundary layer. Experimental values of oxidizer and fuel mass flux are enforced as boundary conditions, on the inlet and grain surfaces, respectively. The remaining chamber walls are modeled as adiabatic. At the outlet, a supersonic outflow boundary conditions is set up. Figure 7 shows the computed temperature and concentration of water vapor, as representative radiating species. Typical hybrid rocket diffusion flames with values of temperature of about 3770 K are found. Water vapor appears more concentrated in the reaction zone, with molar fractions of about 0.26. The flame zone, that exhibits both the highest temperature and concentration of radiating species is therefore confirmed the main source of thermal radiation toward the fuel grain.

A comparison between pressure traces along the chamber axis is given in Fig. 8. Because of the lack of modeling of the post–chamber details, a lower mixing is computed. This results in under predictions of chamber pressure of 7.2% and 20.1% for test case 1 and 2, respectively, in agreement with characteristic velocity efficiencies in Table 1.

Once CFD simulations are completed, the obtained data are provided as input for the DTM simulations. A discretization consisting in 256 rays for each calculation point and a step of 1 mm for each ray, is used after performing convergence analyses for both parameters. As previously mentioned, the minimum elevation angle of line–of–sights is limited according to the geometric FOV. In addition, the wall emissivity is assumed equal to unity, to properly allow to evaluate transmission through both gaseous and window layers separating the combustion chamber from the optical fiber core. The computed wall heat flux profiles are shown in Fig. 9.

By keeping the values at mid–post chamber location, that is about 0.203 m downstream of the inlet section, the computed wall heat fluxes shown in Table 4 are obtained.

DOI: 10.13009/EUCASS2017-149

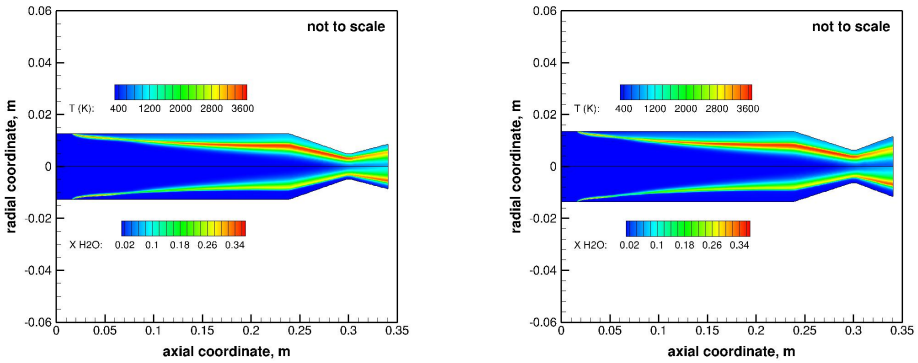

(a) test case 1 (b) test case 2

Figure 7: Computed temperature and water vapor molar fraction fields.

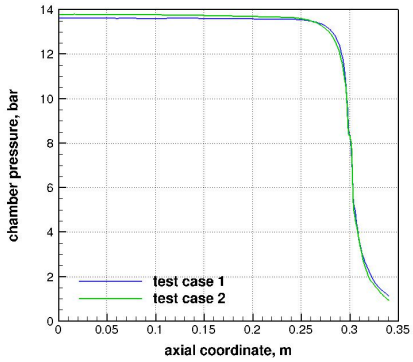

Figure 8: Computed chamber pressure profiles.

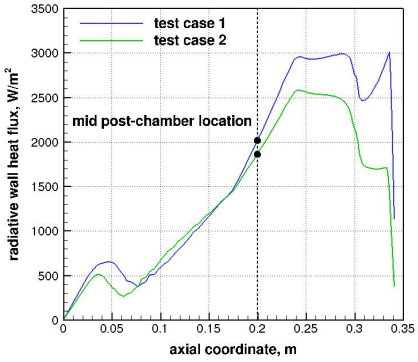

Figure 9: Computed radiative wall heat flux profiles.

Table 4: Computed radiative wall heat fluxes.

TC	$q_{w,rad}$, W/m^2
1	2098.72
2	1927.85

DOI: 10.13009/EUCASS2017-149

A mismatch is found between measurements and computations. Different possible source of uncertainty that can justify such disagreement are however identified.

A first source of uncertainty is given by the absorption properties of the gas into the hole for emission spectra acquisition. Notice that such gaseous layer is important in the absorption of radiative energy toward the spectrometer because of its depth comparable to the port diameter at mid burning time. Moreover, the relatively cold and high fuel–rich conditions in the region near the hole can significantly contribute to make the transmission across the layer lower than assumed in computations. The absorption coefficient of the gaseous layer, in fact, can results higher than the one used in estimating the radiative wall heat flux, both because of a lower temperature in the hole with respect to that computed at wall interface and because of a non–null soot volume fraction due to high fuel concentrations. If for example the contribution of soot,[11,15]

$$\kappa_s = \frac{3.915 C_k}{C_2} f_v T \quad , \quad \text{with} \;\; C_k = 7 \;\; \text{and} \;\; C_2 = 1.439 \times 10^{-2} \;\text{m K} \tag{11}$$

is included in the absorption coefficient, a good agreement between computed and measured radiative wall heat fluxes can be achieved. In fact, radiative wall heat fluxes of 13.88 W/m^2 and 55.08 W/m^2 are found by considering uniform soot volume fractions f_v of 1.2×10^{-4} and 1.8×10^{-4} for test case 1 and 2, respectively. Such values are feasible for a very fuel–rich region since, according to literature data,[7,12] soot volume fractions roughly in between 10^{-6} and 10^{-5} are expected for the pressure level attained in the present combustion chamber. Notice also that in Eq. (11) the temperature of soot T is assumed equal to that of the gas mixture owing to the very small size of soot particles, implying a very high area to volume ratio.[37]

A second source of uncertainty is given by the strong sensitivity of the computed radiative wall heat flux to the actual FOV angle. Figure 10 shows a normalized scaling law of the computed radiative wall heat flux with FOV semi–aperture angle, i.e. θ_1, where a roughly quadratic dependence for both test cases is found.

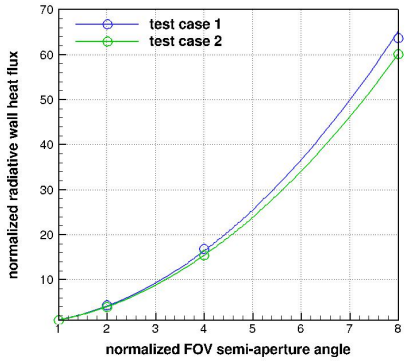

Figure 10: Sensitivity analysis of computed radiative wall heat flux to FOV semi–aperture angle.

Small misalignments of the optical fiber core, as well as shadowing effects associated to soot deposition, can slightly change the FOV angle and accordingly produce significant errors in the rebuilding of experimental data. In particular, numerical results can approach experimental data if θ_1 is reduced to about 1/8 of the value previously assumed.

An important aspect to be stressed is that soot formation and deposition, as verified on the window surface in post–firing inspections, can simultaneously contribute to enhance the absorption properties of the gaseous layer and to reduce the FOV angle, with potentially strong deleterious effects on the agreement between measurements and computations. A possible indication of the role played by the presence of soot in the mismatch between experiments and simulations can be found in the higher disagreement found for test case 2, when a lower mixture ratio is envisaged, and hence a higher presence of soot is expected. In support of this, notice that while the measured value for test case 2 is lower than in test case 1, the computed radiative wall heat flux appears almost unchanged for the two firing tests.

Although for the mentioned reasons a full validation of the model is not allowed by the present experimental conditions, the code is finally employed to produce an estimate of the radiative wall heat flux that there would be at mid post–chamber location if no modification introduced for spectroscopy was present. By leaving aside both FOV restrictions and layers transmission, a value of about 0.1 MW/m^2 is found for both test cases. Such value corresponds to a global emissivity of about 0.1, which underlines a strongly non–black behavior for gaseous media of this class of paraffin–based HREs, i.e. employed chamber pressures and port diameters.

Although results need surely to be improved, the foundations of a combined approach between experimental diagnostic and numerical methods for studying radiative heat transfer in paraffin–based HREs have been drawn. Many

DOI: 10.13009/EUCASS2017-149

lessons have been learned on both numerical and experimental sides. For a more reasonable comparison a detailed soot model should be included in both CFD and DTM codes, because of the probably high importance of soot absorption in the near wall region, where the spectroscopy instrumentation is set up. A detailed description of the post–chamber geometry appears also a way to better capture the actual mixing and conditions near the post–chamber wall. To get measurements much closer to the actual radiative heat flux experienced at post–chamber wall a low aspect ratio hole design is suggested to simultaneously enlarge the FOV angle and enhance transmission through the gaseous layer. A spectrometer able to span a wide range of wavelengths in the infrared domain is also recommended to minimize the extrapolation of the emission spectra and hence any source of error arising from the fitting procedure.

7. Conclusions

Both spectroscopy measurements and discrete transfer method computations have been employed to define possible approaches in evaluating the radiative heat transfer as a driving mechanism for fuel regression rate in paraffin–based hybrid rocket engines. A gaseous–oxygen/paraffin–wax lab–scale hybrid rocket engine with an optical port at mid–post chamber location has been designed and tested for the purpose. The experimental radiative wall heat flux has been obtained by integrating over wavelengths the gathered emission spectra. Before that, a suitable fitting procedure with Planck's law has been employed to take into account the contribution of higher wavelengths. The numerical radiative wall heat flux, on the other hand, has been obtained by integrating the radiative transfer equation within the whole thrust chamber domain with local conditions provided by computational fluid dynamic solutions. Both geometric limitations of the field of view and transmission through layers associated to the measurement setup have been suitably included in the computation. Although a certain mismatch between experiments and simulations has been found, possible sources of error have been clearly identified in the uncertainty of the absorption properties of the gas trapped within the hole for spectroscopy measurements and in the sensitivity of the computed radiative wall heat flux to potential changes in the field of view. In particular, soot formation and deposition, as verified on the window surface in post–firing inspections, can be responsible of both aspects. The basics of the proposed approach have been drawn and many lessons have been learned for future improvements. Modeling soot formation and post–chamber details appears important on the numerical side. A design of low aspect ratios holes for optical access into the post–chamber, together with the use of spectrometers spanning a wider range on infrared wavelengths are, on the other hand, suggested from the experimental point of view.

References

[1] D. Altman and A. Holzman. Overview and history of hybrid rocket propulsion. In K.K. Kuo and M.J. Chiaverini, editors, *Fundamentals of Hybrid Rocket Combustion and Propulsion*, volume 218 of *Progress in Astronautics and Aeronautics*, pages 1–36. AIAA, 2007.

[2] J. D. Anderson. *Hypersonic and High–Temperature Gas Dynamics*. AIAA Education series, 2^{nd} edition, 2006.

[3] B. Betti, F. Nasuti, and E. Martelli. Numerical evaluation of heat transfer enhancement in rocket thrust chambers by wall ribs. *Numerical Heat Transfer Part A: Applications*, 66(5):488–508, 2014.

[4] D. Bianchi, F. Nasuti, and C. Carmicino. Hybrid rockets with axial injector: port diameter effect on fuel regression rate. *Journal of Propulsion and Power*, 32(4):984–996, 2016.

[5] B. Blouri, F. Hamdan, and D. Herault. Mild cracking of high–molecular–weigth hydrocarbons. *Industrial & Engineering Chemistry Process Design and Development*, 1(24):30–37, 1985.

[6] P. N. Brown, G. D. Byrne, and A. C. Hindmarsh. VODE: a variable–coefficient ODE solver. *SIAM Journal on Scientific and Statistical Computing*, 10(5):1038–1051, 1989.

[7] D. Byun and S. W. Baek. Numerical investigation of combustion with non–gray thermal radiation and soot formation effect in a liquid rocket engine. *International Journal of Heat and Mass Transfer*, 50:412–422, 2007.

[8] B. J. Cantwell, M. A. Karabeyoglu, and D. Altamn. Recent advances in hybrid propulsion. *International Journal of Energetic Materials and Chemical Propulsion*, 9(4):305–326, 2010.

[9] M. Chiaverini. Review of solid–fuel regression rate behavior in classical and nonclassical hybrid rocket motors. In K.K. Kuo and M.J. Chiaverini, editors, *Fundamentals of Hybrid Rocket Combustion and Propulsion*, volume 218 of *Progress in Astronautics and Aeronautics*, pages 37–125. AIAA, 2007.

DOI: 10.13009/EUCASS2017-149

[10] A. Coronetti and W. A. Sirignano. Numerical analysis of hybrid rocket combustion. *Journal of Propulsion and Power*, 29(2):371–384, 2013.

[11] J. D. Felske and C. L. Tien. The use of the milne–eddington absorption coefficient for radiative heat transfer in combustion systems. *Journal of Heat Transfer*, 99(3):458–465, 1977.

[12] K. Frederickson, S. P. Kearney, T. W. Grasser, and J. N. Castaneda. Joint temperature and soot–volume–fraction measurements in turbulent meter–scale pool fires. In *47th AIAA Aerospace Sciences Meeting*, Orlando, FL, 2009.

[13] P. Giordano and D. Lentini. Combustion–radiation–turbulence interaction modelling in absorbing/emitting non-premixed flames. *Combustion Science and Technology*, 172(1):1–22, 2001.

[14] S. Gordon and B. J. McBride. Computer program for calculation of complex chemical equilibrium compositions and applications. NASA RP 1311, 1994.

[15] W. L. Grosshandler. A narrow–band model for radiation calculations in a combustion environment. NIST TC 1402, 1993.

[16] S. T. Hsu. *Engineering Heat Transfer*. Van Nostrand Company, 1963.

[17] M. A. Karabeyoglu, D. Altman, and B. J. Cantwell. Combustion of liquefying hybrid propellants: Part 1, general theory. *Journal of Propulsion and Power*, 18(3):610–620, 2002.

[18] M. A. Karabeyoglu and B. J. Cantwell. Combustion of liquefying hybrid propellants: Part 2, stability of liquid films. *Journal of Propulsion and Power*, 18(3):621–630, 2002.

[19] M. A. Karabeyoglu, B. J. Cantwell, and D. Altman. Development and testing of paraffin–based hybrid rocket fuels. In *37th AIAA/ASME/SAE/ASEE Joint Propulsion Conference*, Salt Lake City, UT, 2001.

[20] M. A. Karabeyoglu, G. Zilliac, B. J. Cantwell, S. DeZilwa, and P. Castellucci. Scale–up tests of high regression rate paraffin–based hybrid rocket fuels. *Journal of Propulsion and Power*, 20(6):1037–1045, 2004.

[21] M. Lazzarin, F. Barato, A. Bettella, and D. Pavarin. Computational fluid dynamics simulation of regression rate in hybrid rockets. *Journal of Propulsion and Power*, 29(6):1445–1452, 2013.

[22] G. Leccese, D. Bianchi, and F. Nasuti. Modeling of paraffin–based fuels in the simulation of hybrid rocket flowfields. In *52nd AIAA/SAE/ASEE Joint Propulsion Conference*, Salt Lake City, UT, 2016.

[23] G. Leccese, D. Bianchi, and F. Nasuti. Simulations of hybrid rocket flowfields including modeling of fuel pyrolysis and thermal radiation. In *5th Space Propulsion Conference*, Rome, Italy, 2016.

[24] J. Liu and S. N. Tiwari. Radiative heat transfer effects in chemically reacting nozzle flows. *Journal of Thermophysics and Heat Transfer*, 10(3):436–444, 1996.

[25] F. C. Lockwood and N. G. Shah. A new radiation solution method for incorporation in general combustion prediction procedures. *Symposium (International) on Combustion*, 18(1):1405–1414, 1981.

[26] J. J. Marano and G. D. Holder. General equation for correlating the thermophysical properties of n–paraffins, n–olefins, and other homologous series. 3. Asymptotic behavior correlations for thermal and transport properties. *Industrial & Engineering Chemistry Research*, 36(6):2399–2408, 1997.

[27] M. F. Modest. *Radiative Heat Transfer*. Academic Press, 2003.

[28] P. Narsai. *Nozzle Erosion in Hybrid Rocket Motors*. PhD thesis, 2016. Stanford University.

[29] P. Narsai, E. Momanyi, K. Venkataraman, B. Evans, and B. J. Cantwell. Indirect heat flux measurements at the nozzle throat of a hybrid rocket motor. In *51st AIAA/SAE/ASEE Joint Propulsion Conference*, Orlando, FL, 2015.

[30] P. Rivière and A. Soufiani. Updated band model parameters for H_2O, CO_2, CH_4 and CO radiation at high temperature. *International Journal of Heat and Mass Transfer*, 55(13):3349–3358, 2012.

[31] V. Sankaran. Computational fluid dynamics modeling of hybrid rocket flowfields. In K.K. Kuo and M.J. Chiaverini, editors, *Fundamentals of Hybrid Rocket Combustion and Propulsion*, volume 218 of *Progress in Astronautics and Aeronautics*, pages 323–349. AIAA, 2007.

DOI: 10.13009/EUCASS2017-149

[32] N. Serin and Y. Gogus. Navier–Stokes investigation on reacting flow field of HTPB/O_2 hybrid motor and regression rate evaluation. In *39th AIAA/ASME/SAE/ASEE Joint Propulsion Conference*, Huntsville, AL, 2003.

[33] P. R. Spalart and S. R. Allmaras. A one–equation turbulence model for aerodynamic flows. *La Recherche Aerospatiale*, 1:5–21, 1994.

[34] K. J. Stober, G. Leccese, P. Narsai, K. Ozawa, and B. J. Cantwell. Flame emission spectroscopy in a paraffin–based hybrid rocket. In *67th International Astronautical Congress (IAC)*, Guadalajara, Mexico, 2016.

[35] G. Strang. On the construction and comparison of difference schemes. *SIAM Journal on Numerical Analysis*, 5:506–517, 1968.

[36] C. L. Tien. Thermal radiation properties of gases. *Advances in Heat Transfer*, 5:253–324, 1968.

[37] H. Ziebland and R. C. Parkinson. Heat transfer in rocket engines. AGARD 148–71, 1971.